THE JOURNAL OF BIOLOGICAL CHEMISTRY VOL. 285, NO. 34, pp. 26519–26531, August 20, 2010

Probing Pore Constriction in a Ligand-gated Ion Channel by Trapping a Metal Ion in the Pore upon Agonist Dissociation*[S]

Received for publication, January 10, 2010, and in revised form, April 24, 2010 Published, JBC Papers in Press, May 13, 2010, DOI 10.1074/jbc.M110.102327

Ilya Pittel[1], **Dvora Witt-Kehati**[1], **Nurit Degani-Katzav**[1], **and Yoav Paas**[2]

From the Laboratory of Ion Channels, The Mina and Everard Goodman Faculty of Life Sciences, Institute of Nanotechnology and Advanced Materials, Bar-Ilan University, Ramat Gan 52900, Israel

Eukaryotic pentameric ligand-gated ion channels (pLGICs) are receptors activated by neurotransmitters to rapidly transport ions across cell membranes, down their electrochemical gradients. Recent crystal structures of two prokaryotic pLGICs were interpreted to imply that the extracellular side of the transmembrane pore constricts to close the channel (Hilf, R. J., and Dutzler, R. (2009) *Nature* 457, 115–118; Bocquet, N., Nury, H., Baaden, M., Le Poupon, C., Changeux, J. P., Delarue, M., and Corringer, P. J. (2009) *Nature* 457, 111–114). Here, we utilized a eukaryotic acetylcholine (ACh)-serotonin chimeric pLGIC that was engineered with histidines to coordinate a metal ion within the channel pore, at its cytoplasmic side. In a previous study, the access of Zn^{2+} ions to the engineered histidines had been explored when the channel was either at rest (closed) or active (open) (Paas, Y., Gibor, G., Grailhe, R., Savatier-Duclert, N., Dufresne, V., Sunesen, M., de Carvalho, L. P., Changeux, J. P., and Attali, B. (2005) *Proc. Natl. Acad. Sci. U.S.A.* 102, 15877–15882). In this study, the interactions of Zn^{2+} with the pore were probed upon agonist (ACh) dissociation that triggers the transition of the receptor from the active conformation to the resting conformation (*i.e.* during deactivation). Application of Zn^{2+} onto ACh-bound open receptors obstructed their pore and prevented ionic flow. Removing ACh from its extracellular binding sites to trigger deactivation while Zn^{2+} is still bound led to tight trapping of Zn^{2+} within the pore. Together with single-channel recordings, made to explore single pore-blocking events, we show that dissociation of ACh causes the gate to shut on a Zn^{2+} ion that effectively acts as a "foot in the door." We infer that, upon deactivation, the cytoplasmic side of the pore of the ACh-serotonin receptor chimera constricts to close the channel.

Eukaryotic pLGICs[3] (also called Cys-loop receptors) constitute a superfamily of transmembrane receptors located at the cell surface of excitable neuronal and muscle cells. There, they mediate rapid transport of ions, such as Na^+, K^+, Ca^{2+}, or Cl^-, down their electrochemical gradients to alter the membrane potential or to enable a rise in intracellular Ca^{2+}. The five subunits of pLGICs are radially aligned around the axis of ion permeation pathway to form a channel activatable by neurotransmitters such as ACh, serotonin, γ-aminobutyric acid, glycine, glutamate, or histamine that bind to an extracellular ligand-binding domain (LigBD) (Fig. 1*A*) (1–7).

Although it is well accepted that loops located at the LigBD-channel interface mediate movements of the pore-lining helices (M2s) (8–16), the specific M2 motions that open and close pLGICs are widely debated. Cryo-electron microscopy images of open and closed conformations of the nicotinic ACh receptor (nAChR) from *Torpedo marmorata* gave rise to the concept of gating motions, in which rotations along the longitudinal axis of the M2 segments open or close a mid-pore hydrophobic barrier (17, 18). State-dependent accessibilities of cysteines, histidines, or lysines substituted along the M2s to methanethiosulfonates, Zn^{2+} or protons, have excluded channel gating via rotations (19–23). It was further suggested that rigid body tilting (21) or small scale dilation (23) motions of the M2s gate the pore of an ACh-serotonin receptor chimera or a muscle nAChR, respectively. Several computational simulations suggested that the opening and closing of pLGICs depend on "global quaternary twist" motions (24, 25), rotations (26, 27), or rotations combined with either tilting (28) or bending vibrations (29) of the M2s. In contrast to these computational simulations, recent x-ray crystal structures of two different prokaryotic pLGICs, one displaying a closed pore conformation (30) and another with a potentially open pore conformation (31, 32), suggest that the pore-lining helices rigidly tilt to gate the channel. Yet, a major difference between the tilting gating motions suggested for the prokaryotic channels and those suggested for a eukaryotic pLGIC (21) emerges. In the case of the prokaryotic channels, the putative gating process involves the opening of a barrier to ions at the extracellular side of the pore (30–32), whereas functional studies in eukaryotic pLGICs indicate that activation involves opening of a barrier located at the cytoplasmic side of the pore (19–21, 33).

Here, we used eukaryotic pLGICs that have an engineered capacity to coordinate a metal ion at the cytoplasmic side of their pore (21). In a previous study the accessibility of the engineered histidines to Zn^{2+} ions was probed before or after activation (21), but in this study we detect Zn^{2+} ion trapping inside the pore upon agonist dissociation. This allows us to infer about a constriction motion that takes place during deactivation of a eukaryotic pLGIC.

* This work was supported by the Wolfson Family Foundation and the Israel Science Foundation Grants 812/07 and 1645/07.

[S] The on-line version of this article (available at http://www.jbc.org) contains supplemental "Experimental Procedures," Figs. S1–S3, and additional references.

[1] These authors contributed equally to this work.

[2] To whom correspondence should be addressed. Tel.: 972-3-5317968; Fax: 972-3-7363657; E-mail: paasyo@mail.biu.ac.il.

[3] The abbreviations used are: pLGIC, pentameric ligand-gated ion channel; $5HT_{3A}R$, 5-hydroxytryptamine (serotonin) receptor type 3A; ACh, acetylcholine; LigBD, ligand-binding domain; nAChR, nicotinic acetylcholine receptor; AChBP, ACh-binding protein; nAChR, nicotinic ACh receptor.

EXPERIMENTAL PROCEDURES

Single-Channel and Macroscopic Patch-Clamp Recordings—For recordings, HEK-293T cells were seeded on glass coverslips (13-mm diameter) that had been coated with poly-L-lysine (20 μg/ml). Coverslips were placed in 35-mm plates, and the cells were transfected (by the calcium phosphate technique) with pIRES-CD8 (0.5 μg), as a marker for successful transfection, together with the pcDNA3-receptor (1.5 μg) per plate. Transfected cells were visualized using beads coated with anti-CD8 antibodies (Invitrogen). Recordings were performed 48–72 h following transfection. The cell-attached configuration of the patch-clamp recording technique was used for single-channel recordings. The patch pipettes were prepared from borosilicate glass (Warner Instrument Corp.) using a PC-10 puller (NARISHIGE Group). The electrodes were coated with Sylgard to reduce pipette capacitance, and their resistance was 6–10 megohms when filled with the pipette solution. The bath solution contained (in mM) the following: 140 NaCl, 2.8 KCl, 2 $CaCl_2$, 2 $MgCl_2$, 10 glucose, 10 HEPES, adjusted to pH 7.35 with NaOH (310 mosM). The pipette solution contained (in mM) the following: 1 ACh, 140 sodium isethionate, 2.8 KCl, 10 glucose, 10 HEPES, adjusted to pH 7.35 with NaOH (310 mosM). Zinc acetate (10 μM) was added to the pipette solution whenever the effect of Zn^{2+} was examined. Single-channel currents were recorded using an Axopatch 200B patch clamp amplifier and a Digidata 1440A interface (Molecular Devices). Acquisition of recording data were performed at 10 kHz, and recordings were low-pass filtered at 1 kHz through a four-pole Bessel filter on the Axopatch 200B amplifier.

Data acquisition and analysis were performed using the pClamp 10.0 software package (Molecular Devices). Single-channel events were detected by the half-amplitude threshold criterion using the Clampfit 10.0 program implemented within pClamp 10.0. The distributions of open and closed times were fitted with a single or two exponentials. Single-channel current amplitudes were measured as the mean of a Gaussian distribution fitted to the amplitude distribution.

Measurements of macroscopic currents were performed basically as in Sunesen *et al.* (34). The bath solution contained (in mM) the following: 140 NaCl, 2.8 KCl, 2 $CaCl_2$, 2 $MgCl_2$, 10 glucose, 10 HEPES, adjusted to pH 7.35 with NaOH. Patch pipettes had 6–10 megohm resistance when filled with a solution containing (in mM) the following: 130 CsCl, 4 $MgCl_2$, 4 Na_2ATP, 1 EGTA, 10 HEPES, adjusted to pH 7.35 with CsOH. ACh was applied onto the cell by using the VC-77SP fast step system (Warner Instruments) combined with N_2 pressure of 3–4 p.s.i.

Computer-assisted Homology Modeling—An oligomeric model of the LigBD of chimera H-5′ was built by using the carbachol-liganded ACh-binding protein (35) (AChBP, Protein Data Bank code 1UV6) as a quaternary structure template. To this end, the N-terminal sequence of the chimeric subunit was threaded throughout the atomic coordinates of each AChBP chain, according to the sequence alignment shown in supplemental Fig. S1. The resulting three-dimensional alignment was submitted for oligomeric modeling to the SWISS-MODEL Repository, a data base for theoretical protein models. After energy minimization with GROMOS96, the best three-dimensional structural alignment between the pentameric LigBD and the AChBP gave a root mean square difference of 0.38 Å for 3880 backbone atoms of 970 counterpart amino acids. Note that the modeled LigBD and the AChBP have 1030 and 1025 amino acids, respectively. Thus, 60 amino acids from the LigBD and 55 amino acids from the AChBP are not included in this root mean square difference calculation. The final model was then docked onto the structural model previously published for the transmembrane channel domain of chimera H-5′ (21). Hence, the backbone carbon atom (C′) of Arg-206 of each LigBD subunit was positioned 1.35 Å away from the backbone nitrogen atom of Pro-207 of the counterpart subunit in the channel domain (see supplemental Fig. S1 for amino acid numbers). The backbone was then ligated *in silico* to obtain an oligomeric receptor-channel structure, and energy minimization was performed once again with GROMOS96. No clashes have been observed between amino acids or between the backbone and amino acids, within the individual subunits or at the intersubunit interfaces. The models of the closed and open conformations built by Paas *et al.* (21) were used for Zn^{2+} docking.

Data Analysis and Computation—Data analysis and computation relating to dissociation constants, EC_{50} values, and Hill coefficients were carried out using GraphPad Prism.

In the case of ^{3}H-αBTx binding assays, curves were fitted to the data points by a nonlinear regression using Equation 1,

$$B = \frac{B_{max} \cdot [^3\text{H-}\alpha\text{BTx}]}{K_D + [^3\text{H-}\alpha\text{BTx}]} \quad \text{(Eq. 1)}$$

where B is the bound ^{3}H-αBTx; B_{max} is the maximal binding of ^{3}H-αBTx; [^{3}H-αBTx] is the concentration of radiolabeled toxin; and K_D is the dissociation constant, which equals the concentration of toxin required to reach half-maximal binding.

In the case of inhibition of ^{3}H-αBTx binding by small agonists (ACh or nicotine), curves were fitted to the data points by a nonlinear regression using the Hill Equation 2,

$$\frac{B}{B_{max}} = 1 - \frac{1}{1 + 10^{(\log K_i - \log[\text{agonist}]) \cdot n_H}} \quad \text{(Eq. 2)}$$

where B is the bound [^{3}H]α-BTx; B_{max} is the maximal binding of [^{3}H]α-BTx; K_i is the agonist inhibition constant; [agonist] is the ACh or nicotine concentration and n_H is the Hill coefficient.

In activation experiments where EC_{50} values were determined electrophysiologically, curves were fitted to the data points by a nonlinear regression using the Hill Equation 3,

$$\frac{I}{I_{max}} = \frac{1}{1 + 10^{(\log EC_{50} - \log[\text{agonist}]) \cdot n_H}} \quad \text{(Eq. 3)}$$

where I is the current response; I_{max} is the maximal current response; EC_{50} is the agonist concentration necessary to obtain 50% of maximal current response; [agonist] is the ACh concentration, and n_H is the Hill coefficient.

For the two-state allosteric model, Equation 4 was used,

$$F_{active} = \frac{1}{1 + L\left\{\frac{1 + \frac{[ACh]}{K_D r}}{1 + \frac{[ACh]}{K_D a}}\right\}^n} \quad \text{(Eq. 4)}$$

where F_{active} is the fraction of the total receptor population in the active state; [ACh] is the concentration of the activator (ACh) for which there are "*n*" equivalent binding sites, each binds ACh with a microscopic dissociation constant K_Dr in the resting state, and K_Da in the active state. *L* is the equilibrium constant of the two states in the absence of ACh; it is equal to the total resting/active receptor ratio. The *L* value was determined based on functional experiments, as described in the legend to supplemental Fig. S2, *E–H*. Note that Equation 4 is equivalent to Equation 1 in Ref. 36, where the resting state is called the "*T*" state and the active state is called the "*R*" state.

To determine the activation time constants, the current rise of the traces (like those shown in Figs. 4 and 5) was best fitted with a single exponential time course by using Equation 5,

$$Y = A \cdot e^{(-t/\tau)} + C \quad \text{(Eq. 5)}$$

where *A* is the current amplitude; *t* is the time; τ is the time constant, and *C* is the constant *y* offset.

The zinc association rate constant shown in Scheme 1 (see text) was calculated according to the explanation provided under "Results" (under "Single-Channel Recordings Show Fast and Slow Zn^{2+}-blocking Events"), as in Equation 6,

$$k_{+Zn} = \frac{\frac{1}{2.2 \cdot 10^{-3}\text{s}} - \frac{1}{2.9 \cdot 10^{-3}\text{s}}}{10^{-5}\text{M}} \approx 1.1 \cdot 10^{7}\text{s}^{-1}\text{M}^{-1} \quad \text{(Eq. 6)}$$

Statistical Analysis—Unless stated otherwise, *p* values correspond to two-tailed paired *t* tests.

The following methods are provided in the supplemental material under supplemental Experimental Procedures: Chimeras and Mutants, Transfection of Cultured Cells and Cell Harvesting, Membrane Preparation, Ligand Binding Assays, and Electrophysiology in *Xenopus* Oocytes.

RESULTS

Structural Properties of the Chimeric Receptors Used Here and Their Capability to Interact with Zn^{2+}—The receptors employed here assemble as homopentamers, and each subunit is a fusion polypeptide that consists of the extracellular N-terminal segment of the nAChR α7 subunit fused to the transmembrane and intracellular C-terminal segment of the serotonin receptor $5HT_{3A}$ subunit (37). Therefore, this chimeric α7–$5HT_{3A}$R responds to ACh, which binds to the LigBD to open a channel of a serotonin receptor. The chimeric α7–$5HT_{3A}$R was further mutated as follows. (i) Following Dang *et al.* (38), a V13′T mutation was introduced in the M2 pore-lining segment to eliminate the desensitization capacity of the chimera. (ii) The M1-M2 connecting sequence was replaced by the homologous sequence of the β subunit of the *Caenorhabditis elegans* glutamate-gated ion channel (21). A homology model of this chimera (H-5′) is shown in Fig. 1*A*. The replacement of the M1-M2 sequence resulted in a histidine residue at position −5′; thus, upon receptor assembly, five histidines have become organized around the ion permeation pathway (Fig. 1*B*) (21). Note that the replacement of the M1-M2 segment also removed a glutamate residue from position −1′, because the replacing M1-M2 segment naturally contains a glycine residue at this position (Fig. 1*C*). As such, the negatively charged ring at position −1′ was neutralized and could not serve as a potential metal-binding site, whereas the cytoplasmic (bottom) side of the ion channel pore has been equipped with a metal-binding ring consisting of five imidazole groups. Moving the histidine downstream, along the replacing M1-M2 segment, provided a metal-binding ring slightly higher in the pore (chimera H-2′) (Fig. 1, *B* and *C*, and Fig. 6, *right side*). We further designed control mutants that contain the aforementioned changes, with

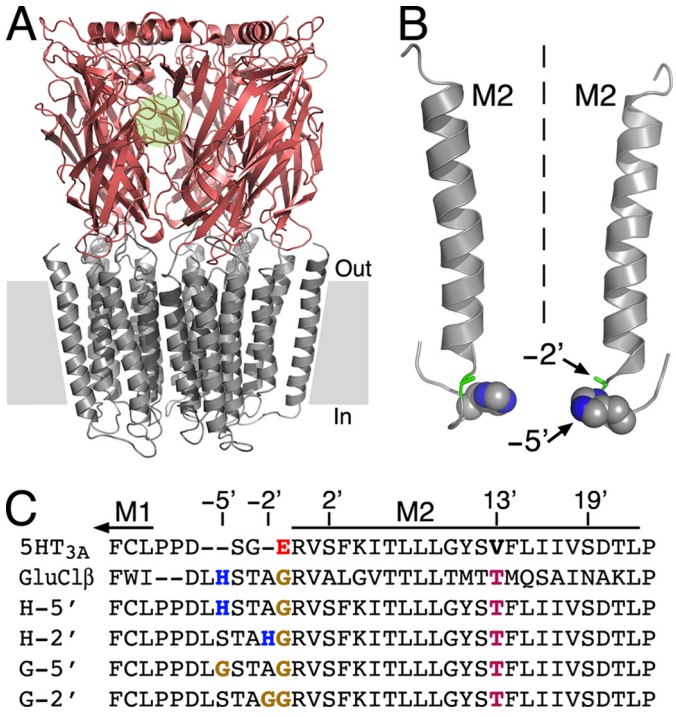

FIGURE 1. **Structural properties of the chimeric pLGICs used here.** *A*, side view of a three-dimensional homology model of chimera H-5′, which consists of the extracellular LigBD of the α7 nAChR (*reddish*) and the transmembrane channel domain of the $5HT_{3A}$ serotonin receptor (*gray*). One of five intersubunit ACh-binding pockets is depicted by a *green circle*. The channel domain consists of 20 helices (4 from each subunit). *Gray rectangles* depict the lipid bilayer. The three-dimensional structure of the intracellular domain (assembled from five M3-M4 connecting sequences) is absent because most of it does not have a counterpart template structure. In various eukaryotic pLGICs, this domain was shown to interact with cytoplasmic proteins to mediate receptor clustering and trafficking (85, 86). *B*, shown are two of five transmembrane M2 segments that line the ion channel pore. *Dashed line* indicates the 5-fold axis of symmetry, which is also the axis of ion permeation pathway. A space-filling model of the histidines at position −5′ is shown with carbon and nitrogen atoms colored in *gray* and *blue*, respectively. The alanines at position −2′ are shown as *green sticks*. Hydrogens were removed for clarity. *C*, amino acid sequence alignment of the M2 segments of the chimeras studied here and the receptors whose channel-forming sequences were utilized for the chimeric design. *$5HT_{3A}$*, a subunit of 5-hydroxytryptamine (serotonin)-activated cationic channel from mouse (Swiss-Prot accession number P23979); *GluClR-β*, β subunit of a glutamate-activated chloride channel from *C. elegans* (Swiss-Prot accession number Q17328). Positions are numbered relatively to the first amino acid of M2 (R0′).

one exception being a glycine instead of a histidine at either position −5′ (chimera G-5′) or position −2′ (chimera G-2′) (Fig. 1*C*). We have used these Gly-containing control chimeras to determine whether the effects of Zn^{2+} are specific to the presence of the engineered histidines.

In a previous article, Paas *et al.* (21) determined the capacity of the aforementioned chimeras to interact with Zn^{2+} ions before and after activation. For clarity, supplemental Fig. S2, *A* and *B*, shows again the dose-dependent inhibitory effect that externally applied Zn^{2+} ions have on the open state of chimeras H-5′ and H-2′, respectively. The Zn^{2+} inhibition constants (K_i) at −80 mV were (in μM) as follows: 30 ± 4.8 and 80 ± 12 (mean ± S.D., N = 8 and 6) for chimeras H-5′ and H-2′, respectively (21). The supplemental Fig. S2, *C* and *D*, shows that the glycine-containing control chimeras, G-5′ and G-2′, were inhibited to much lesser extent (inhibition of 27 ± 2% and 19 ± 5.6% at 1 mM Zn^{2+} (mean ± S.D., N = 5 and 4), respectively (21)). We do not know what is the origin of this weak inhibition; however, we do not exclude a weak inhibitory effect by Zn^{2+} interacting with the LigBD. Indeed, it was recently shown that a pentameric glycine-gated ion channel is strongly inhibited by Zn^{2+} that binds to the underlined amino acids of the HFHEIT sequence in the LigBD (39). Notably, at the homologous positions of the nAChR-α7 subunit (the donor of the LigBD in our chimeras), there are four side chains that could potentially interact with divalent metal cations (RFDATF; see sequence alignment in Ref. 40). In any event, based on supplemental Fig. S2, *A–D*, and other results by Paas *et al.* (21), it was concluded: (i) in the open conformation, a ring of five histidines at either position −5′ or −2′ is accessible for interactions with externally applied Zn^{2+} ions, and (ii) binding of Zn^{2+} blocks the open pore, presumably because a bound Zn^{2+} ion sterically interferes with the flow of other ions through the ion permeation path.

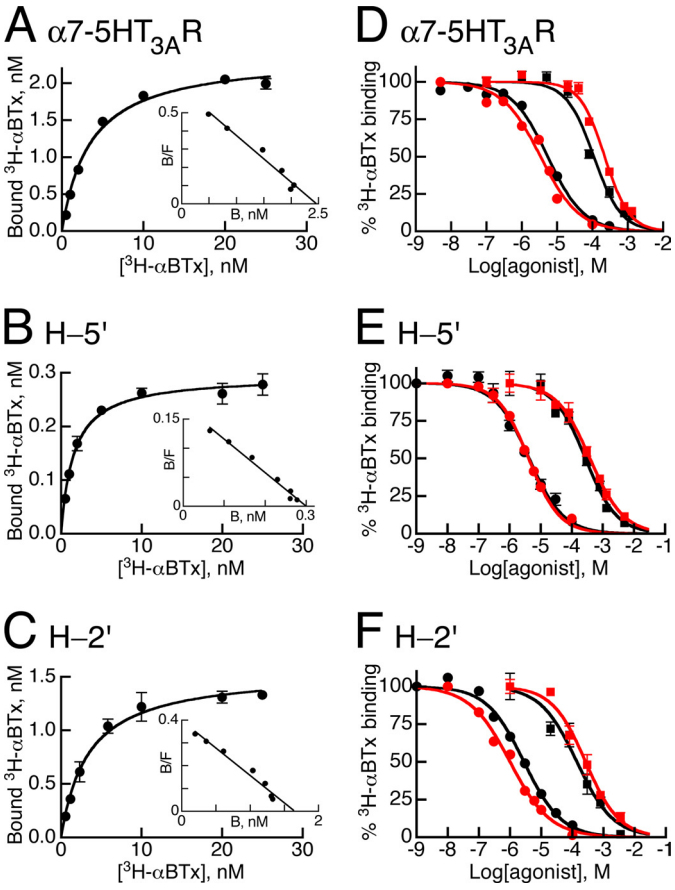

FIGURE 2. **Ligand binding properties of the chimeric receptors α7–5HT$_{3A}$R, H-5′, and H-2′.** *A–C*, saturation curves of ^{3}H-αBTx binding to the chimeras indicated in the panels. *Insets* correspond to Scatchard analyses showing maximal αBTx binding (B_{max} in nM) of 2.5 ± 0.3, 0.3 ± 0.02, and 1.65 ± 0.2 (mean ± S.D.) for chimeras α7–5HT$_{3A}$R, H-5′, and H-2′, respectively. *D–F*, ^{3}H-αBTx binding to the indicated chimeras in the presence of increasing concentrations of ACh (*squares*) or nicotine (*circles*). Throughout *D–F*, the competitive binding assays were performed in the absence (*black curves*) or presence (*red curves*) of 1 mM Zn^{2+}. The ^{3}H-αBTx concentration was 4–5 nM, which approximates the toxin dissociation constants (K_D values in Table 1).

Ligand Binding Properties of the Chimeric Receptors—αBTx belongs to a family of α-neurotoxins that stabilize ACh receptors in a nonconducting state (41–43) by interacting with the ACh-binding pockets to sterically interfere with agonist binding (5, 44–49). αBTx binds to the brain α7 nAChR with nanomolar affinities (50). Our chimeras have the LigBD of the α7 nAChR, which binds small agonists like ACh or nicotine with low affinities (K_D of tens or few micromolars, respectively) (50, 51). Here, we characterized the binding affinity of the chimeras for αBTx (K_D values) and the capacity of ACh and nicotine to competitively inhibit ^{3}H-αBTx binding (K_i values).

Fig. 2, *A–C*, shows saturation curves of ^{3}H-αBTx binding to the α7–5HT$_{3A}$R and chimeras H-5′ and H-2′. The resulting dissociation constants (K_D) are shown in Table 1. The similar K_D values indicate that the three receptors bind αBTx with virtually the same affinity. The linear fits of the Scatchard plots (small insets) indicate that in each chimera the binding sites that do accommodate αBTx are identical.

As a next step, equilibrium binding assays were employed to determine the K_i values of ACh and nicotine. Fig. 2, *D–F* (*black curves*), shows binding of ^{3}H-αBTx (at its K_D concentration) in the presence of increasing concentrations of ACh or nicotine.

TABLE 1

Ligand binding properties of the α7–5HT$_{3A}$R and chimeras H-5′ and H-2′

K_D, K_i, and n_H are the dissociation constant, inhibition constant, and Hill coefficient, respectively. Data are means ± S.D. of at least three independent experiments, each performed in triplicate. Two-way analysis of variance between the affinities of the agonists for the three chimeras in the absence and presence of Zn^{2+} gave p = 0.67 and p = 0.27 in the case of ACh and nicotine, respectively.

Receptor	αBTx, K_D	ACh				Nicotine			
		−Zinc		+Zinc		−Zinc		+Zinc	
		K_i	n_H	K_i	n_H	K_i	n_H	K_i	n_H
	nM	μM		μM		μM		μM	
α7–5HT$_{3A}$R	4.2 ± 0.7	143 ± 41	1.2 ± 0.1	201 ± 57	1.3 ± 0.1	3.2 ± 1.6	1.3 ± 0.3	3.8 ± 0.4	0.9 ± 0.1
H-5′	3.3 ± 2.4	201 ± 53	1.1 ± 0.2	324 ± 101	0.9 ± 0.1	3.2 ± 0.9	0.8 ± 0.1	2.9 ± 1.0	0.8 ± 0.1
H-2′	5.0 ± 2.8	182 ± 69	0.8 ± 0.1	224 ± 56	0.7 ± 0.1	3.7 ± 1.2	0.9 ± 0.1	1.8 ± 0.8	1.0 ± 0.2

TABLE 2

Affinity constants derived from channel activity

K_Dr, K_Da, and K_Dd are the microscopic ACh dissociation constants of the resting, active, and desensitized states, respectively. For the α7–5HT$_{3A}$R, these constants were previously determined based on a three-state allosteric model (indicated by asterisks (55)); they are compared with the constants determined here for chimeras H-5′, H-2′, and H-2′$^{(RRR\rightarrow QDA)}$ that, unlike the α7–5HT$_{3A}$R, do not undergo desensitization.

Receptor	Fitting by the Hill equation		Microscopic constants (allosteric models)		
	ACh-EC$_{50}$	n_H	K_Dr	K_Da	K_Dd
	μM		μM	μM	μM
α7–5HT$_{3A}$R	68 ± 24 (7)[a]	1.4 ± 0.2[a]	88.0*	2.25*	1.6*
H-5′	10 ± 2.8 (6)[a]	2.2 ± 0.3[a]	96.0	9.40	
H-2′	5 ± 0.5 (5)[a]	2.4 ± 0.2[a]	98.5	4.40	
H-2′$^{(RRR\rightarrow QDA)}$	15 ± 2.6 (13)[b]	2.7 ± 0.5[b]	104	12.2	

[a] ACh-EC$_{50}$ is the ACh concentration that gives half-maximal current response; n_H is Hill coefficient of activation (mean ± S.D.; number of cells is in parentheses). Data were determined in *Xenopus* oocytes by Paas *et al.* (21).

[b] Data were determined here in HEK293T cells.

Evidently, the α7–5HT$_{3A}$R and chimeras H-5′ and H-2′ display similar ACh- and nicotine-K_i values (Fig. 2, *D–F,* and Table 1, under headings ACh or Nicotine, −Zinc), indicating that these three chimeric receptors share similar affinities for their agonists, ACh and nicotine.

We repeated the competitive binding assays in the presence of Zn^{2+} ions, because Zn^{2+} was used in electrophysiological experiments as a probe that interacted with the ring of five histidines engineered in the channel (described further below). Fig. 2, *D–F* (*red curves*), and Table 1 (under headings ACh or Nicotine, +Zinc) show that Zn^{2+} does not change the binding affinities of ACh or nicotine significantly. The Hill coefficients of ACh or nicotine binding were also not affected by the presence of Zn^{2+} ions in the ligand binding reactions.

In the α7–5HT$_{3A}$R, the ACh-K_i value (Table 1, under −Zinc) is ~2 times higher than the ACh-EC$_{50}$ value derived from electrophysiological experiments (Table 2), in agreement with the ratio obtained previously for this chimera (51). In contrast, for chimeras H-5′ and H-2′, dividing the ACh-K_i values (Table 1, under −Zinc) by the ACh-EC$_{50}$ values in Table 2 gave mean ratios of ~20 and ~36, respectively. This significant difference between the α7–5HT$_{3A}$R and chimeras H-5′ and H-2′ motivated us to explore the allosteric properties of chimeras H-5′ and H-2′, as described below.

Chimeras H-5′ and H-2′ Display Two Main Conformations—The α7–5HT$_{3A}$R is capable of desensitizing (Fig. 3*A*), *i.e.* its activation is followed by channel closing, but the receptor retains a high affinity for the agonist. In contrast, chimeras H-5′ and H-2′ were engineered not to desensitize, so that the pore remains open as long as an agonist is bound (Fig. 3, *B* and *C*). Elimination of desensitization was essential to ensure that any current decline due to interactions of Zn^{2+} with the histidines could not be attributed to desensitization.

Previous studies performed with two different pLGICs have shown that mutations at the mid-pore 9′ position stabilize a so-called "pathologically opened desensitized state," which was permeable to ions and displayed a drastic increase in apparent affinity (*i.e.* ~160-fold decrease in ACh-EC$_{50}$) (52, 53). In these mid-pore mutants, the Hill coefficient of activation also changed significantly; it decreased from values ranging from 1.5 to 2.0 toward a value of 1 (52, 53). In contrast, the ACh-EC$_{50}$ values of chimeras H-5′ and H-2′ decreased moderately (by ~7 and ~14 respectively, compared with the α7–5HT$_{3A}$R), and their Hill coefficients of activation significantly increased (Table 2). These observations suggest that the open state of our chimeras potentially reflects the active state rather than a pathologically opened desensitized state. To ascertain that the chimeric H-5′ and H-2′ receptors indeed isomerize between two dominant states and that their conducting conformation corresponds to the active state, we have employed a two-state allosteric model based on the Monod-Wyman-Changeux theory (54) as applied also by Karlin (36) to the nAChR.

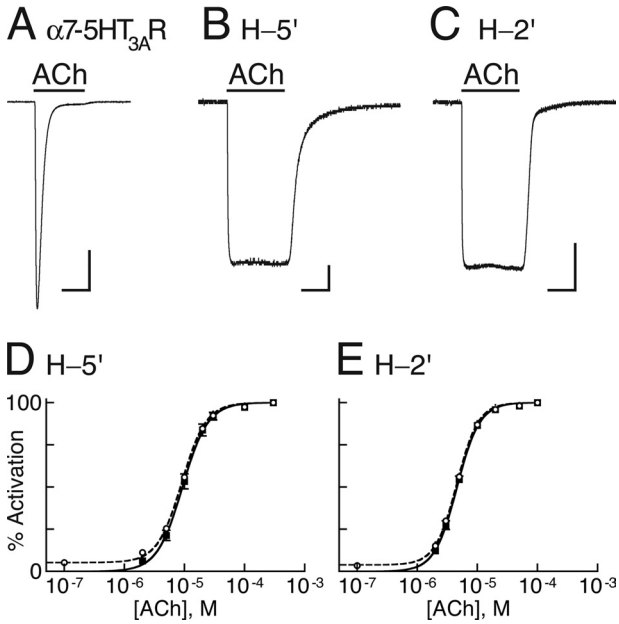

FIGURE 3. **Channel activity and allosteric modeling.** *A–C,* representative inward currents measured at −80 mV and room temperature in *Xenopus* oocytes expressing the indicated chimeras, as a response to saturating concentrations of ACh (300 μM). In each panel, the *horizontal bar* at the bottom corresponds to 3 s, and the *vertical bar* corresponds to 0.5 μA. *D* and *E*, dose-response curves (*continuous black lines*) for the indicated chimeras fitted by the Hill equation (Equation 3) to data points obtained from ACh-elicited steady-state currents (*black squares*). The *dashed curves* were fitted to data points that include the ACh-elicited currents plus the Zn^{2+}-inhibited leak currents (*open circles*). Fitting of the *dashed curves* was performed by using a two-state allosteric model (Equation 4 in "Experimental Procedures") with $n = 5$ binding sites, microscopic ACh dissociation constants for the resting (K_Dr) and active (K_Da) states as provided in Table 2, and equilibrium constants $L = 18$ and $L = 28$ for H-5′ and H-2′, respectively. *L* values were determined as explained in the legend to supplemental Fig. S2, *E–H*.

A two-state allosteric model postulates that the receptor interconverts between two distinct states as follows: a resting state, having a closed channel conformation, and an active state, having an open channel conformation. The equilibrium constant (L), which describes the resting$_0$ ↔ active$_0$ isomerization in the absence of an effector, was determined by analyzing Zn^{2+}-blockable leak currents that we measured in oocytes expressing chimeras H-5′ and H-2′ (*red traces* in supplemental Fig. S2, *E* and *F*; see legend). Because Zn^{2+} had a very little effect on the leak currents recorded from oocytes expressing chimeras G-5′ and G-2′ (supplemental Fig. S2, *G* and *H*), we attribute the Zn^{2+}-blockable currents (supplemental Fig. S2, *E* and *F*) to ions flowing specifically through spontaneously opened H-5′ and H-2′ channels. Assuming five identical ACh-binding sites, activation

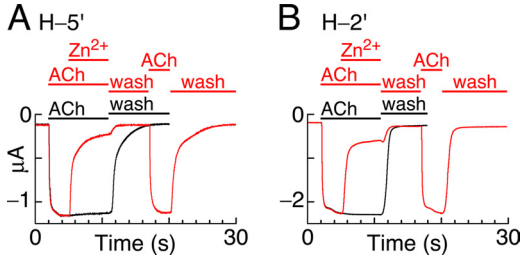

FIGURE 4. **Blocking of open channels by Zn^{2+} in a reversible manner.** *A* and *B*, indicated chimeric receptors (expressed in *Xenopus* oocytes) are activated by saturating concentrations of ACh (300 μM) for 9 s. 3 s after onset of activation, 1 mM Zn^{2+} is added for 6 s to block the open channels (*left side of the red traces*). Then, following a 6-s-long wash of both ACh and Zn^{2+} simultaneously (*1st red wash*), the chimeras were reactivated with ACh (300 μM; *2nd red ACh*) for 3 s, and washed again (*2nd red wash*). The *black traces* are unblocked currents activated by 300 μM ACh for 9 s; they show the maximal nondesensitizing current amplitudes. Recordings were performed at −80 mV and room temperature.

curves simulated based on this two-state allosteric model closely matched the activation Hill curves (Fig. 3, *D* and *E*). The microscopic ACh dissociation constants derived from the two-state allosteric model for the resting state (K_Dr) of chimeras H-5′ and H-2′ were very close to the microscopic dissociation constant characterized previously for the resting state of the α7–5HT_{3A}R chimera (55) (Table 2). The microscopic ACh dissociation constants derived for the active state (K_Da) of chimeras H-5′ and H-2′ were, respectively, ~6 and ~3 times higher than the microscopic ACh dissociation constant characterized previously for the desensitized state (K_Dd) of the α7–5HT_{3A}R (Table 2) (55). These ratios are clearly greater than the K_Da/K_Dd ratio characterized previously for the α7–5HT_{3A}R based on a three-state allosteric model (~1.4 in Ref. 55) (Table 2). It is therefore most likely that chimeras H-5′ and H-2′ do not adopt a desensitized state with higher affinity for agonists than the open state. We conclude that the conducting channel conformation of chimeras H-5′ and H-2′ corresponds to the active conformation; so, the transition of these chimeras from the open state to the closed state corresponds to the active → resting transition typical of the deactivation process.

Triggering Receptor Deactivation Leads to Zn^{2+} Ion Trapping at the Bottom of the Shutting Pore—Fig. 4 (*red traces*) shows that following block of opened channels by a high Zn^{2+} concentration (1 mM), wash out of both ACh and Zn^{2+} simultaneously allows for reactivation of the entire channel population by ACh with similar amplitudes and activation time constants: $\tau = 84 \pm 26$ ms *versus* 72 ± 16 ms (mean ± S.D.; $N = 6$) for the first *versus* second ACh application in H-5′ ($p = 0.36$), and $\tau = 86 \pm 29$ ms *versus* 103 ± 32 ms (mean ± S.D.; $N = 5$) for the first *versus* second ACh application in H-2′ ($p = 0.40$).

Because Zn^{2+} blocks the active open conformation reversibly, the following question may be asked. Will the ring of five histidines trap Zn^{2+} upon pore closure? To answer this question, we induced deactivation of receptors having open, Zn^{2+}-blocked channels. Fig. 5*A* shows a series of current traces (*lined up vertically*) obtained from a continuous experiment done in an oocyte that expresses chimera H-5′. Fig. 5*A, upper trace,* corresponds to the activation by saturating concentrations of ACh followed by a wash. This current response corresponds to the full capacity of activation, where the current reaches a steady state and does not decline as long as ACh is present. The *2nd* to *6th traces* in Fig. 5*A* indicate application protocols where ACh was applied at saturating concentrations until the channel population reached a steady state, and then a high Zn^{2+} concentration (1 mM) was added to the ACh solution. The addition of Zn^{2+} caused current decline to point *a* (*2nd trace* in Fig. 5*A*), which corresponds to ~90% inhibition of the ACh-elicited currents. This indicates that Zn^{2+} blocked most of the open channels. Subsequently, the ACh plus Zn^{2+} solution was replaced by a zinc-containing solution devoid of ACh to remove ACh and to trigger receptor deactivation in the presence of a high Zn^{2+} concentration. This step led to further decline of the current to the base line (*dashed line* in Fig. 5*A*; denoted by *b* in the *2nd trace*), which demonstrates the deactivation of the remaining ~10% unblocked channels. Further reduction in the leak current from *b* to *c* in Fig. 5*A* is attributed to pore blockage of spontaneously opened H-5′ channels (as elucidated above).

Then a solution devoid of both ACh and Zn^{2+} was applied for varying washing periods as indicated by the first "wash" throughout Fig. 5*A*. The return of the current from point *c* in Fig. 5*A* to the base line indicates that during this wash Zn^{2+} dissociated from the spontaneously open channels, and it was washed out of the application bath together with all the free Zn^{2+} ions before ACh reapplication. Reapplication of ACh alone (2nd ACh application in Fig. 5*A*) resulted in currents that were significantly weaker than those elicited by the first ACh application, *i.e.* after a 6-s-long wash (*2nd trace* in Fig. 5*A*), ~70% of the channel population reopened with an activation kinetics ($\tau = 87 \pm 32$ ms) similar to that of the first activation ($\tau = 81 \pm 24$ ms) (mean ± S.D., $N = 5$, $p = 0.75$), but ~30% of the channel population did not conduct current. After a 30-s-long wash (*6th trace* in Fig. 5*A*), ~8% of the channels were still nonconducting. In contrast to the strong inhibitory effect of Zn^{2+} on chimera H-5′, Zn^{2+} weakly inhibited the ACh-elicited currents in the control chimera, which has glycines instead of histidines at position −5′ (Fig. 5*B*). Also, Zn^{2+} did not inhibit the leak currents through the G-5′ mutant. Most importantly, currents have fully recovered upon reactivation of the G-5′ control chimera (Fig. 5*B*).

Together, our observations indicate that, under this experimental protocol (Fig. 5*A*), Zn^{2+} becomes trapped in the pore of chimera H-5′ and stabilizes a nonconducting conformation; this is probably due to strong interactions of Zn^{2+} specifically with the five-imidazole ring inserted at position −5′. Similar results were observed with chimera H-2′ and its G-2′ control mutant (supplemental Fig. S3). Fig. 5*C* provides quantitative analyses for the recovery of the currents; it shows that significant H-5′ and H-2′ channel subpopulations lost their capability to recover when ACh is washed away prior to Zn^{2+} (unlike the case of the control G-5′ and G-2′ chimeras, which were mostly unaffected).

Single-Channel Recordings Show Fast and Slow Zn^{2+} Blocking Events—Chimera H-2′ has the intracellular domain of the 5HT_{3A}R. It was previously shown that receptors having a channel domain assembled from the 5HT_{3A} subunit must carry three specific mutations (RRR → QDA) within the intracellular domain to conduct (with a yet unknown mechanism) detectable single-channel currents (9, 56). These three QDA substitu-

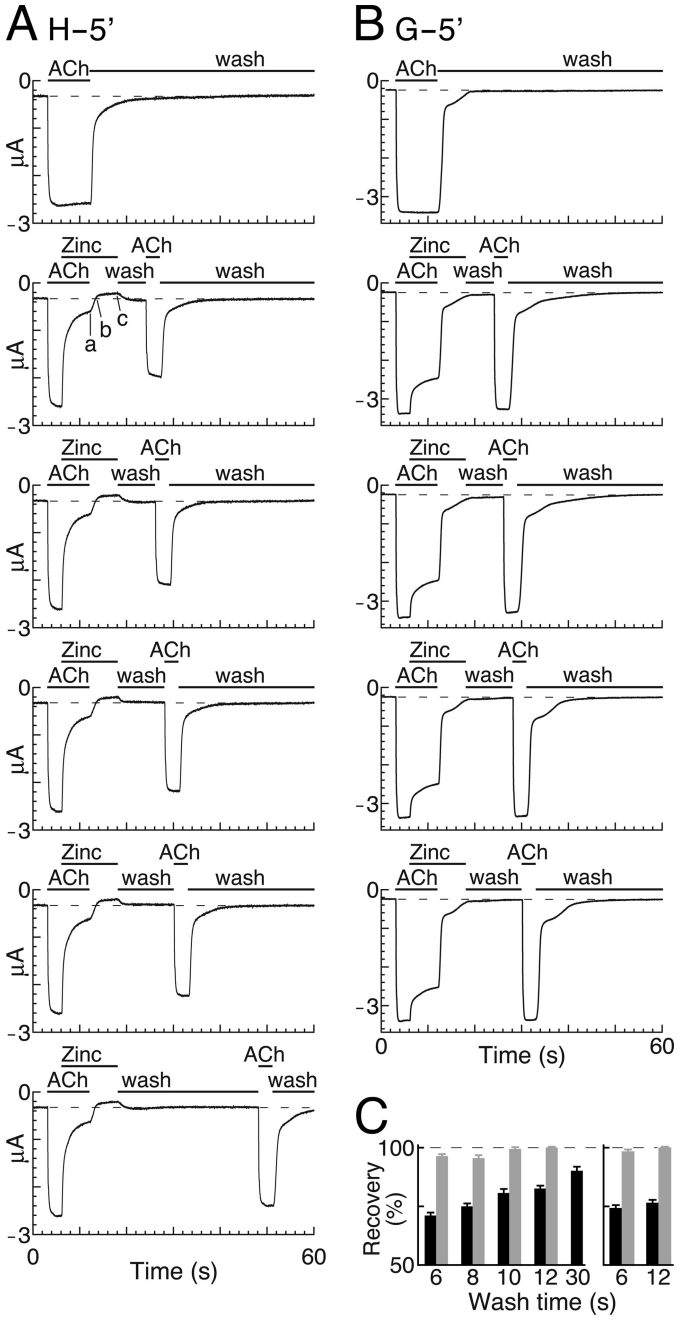

FIGURE 5. **Induction of receptor deactivation in the presence of Zn^{2+} ions.** *A*, six representative current episodes recorded from *Xenopus* oocytes expressing chimera H-5′ are lined up *vertically*. The *1st episode* corresponds to activation by a saturating ACh concentration (300 μM) for 9 s, which shows the maximal nondesensitizing current amplitude. *Dashed line* shows the base line. *2nd* to *6th episodes* show application of an ACh-containing solution (300 μM) for 3 s, which was replaced by a solution that contains both ACh (300 μM) and Zn^{2+} (1 mM) for a further 6 s. The addition of Zn^{2+} led to inhibition of the steady-state current (*decline to point a*). Then, the solution containing both ACh and Zn^{2+} was replaced by a solution containing 1 mM Zn^{2+} without ACh, for further 6-s-long application to remove ACh while leaving Zn^{2+} in the application bath. This step led to further decline of the current to the base line (*point b*) and then to the inhibition of the leak current (from *b* to *c*). The oocyte was then washed with a physiological solution devoid of both ACh and Zn^{2+} for varying time periods (under *1st wash*); within this washing time, the current trace returned from point *c* to the base line. Then, ACh (300 μM) was reapplied for 3 s (under *2nd ACh*), followed by a second wash. Note that after each 60-s-long episode, the oocyte was briefly stimulated for a few times by ACh alone (and washed) until the maximal (primary) amplitude recovered. Recordings were performed at −80 mV at room temperature. *B*, same as in *A* but with a glycine-containing control chimera (G-5′). *C*, histograms of experiments performed as in *A* and *B*. Shown are percentages of current recovery (after the indicated washing times) of the chimeras as follows: H-5′ (*left, black columns*), G-5′ (*left, gray columns*), H-2′ (*right, black columns*), and G-2′ (*right, gray columns*). The recovery of the H-5′ channels significantly differs from that of the G-5′ channels; for 6, 8, 10, and 12 s of wash, $p < 0.0001$; for a 30-s wash of H-5′ compared with a 12-s wash of G-5′, $p < 0.0007$ ($N = 5$). The recovery of the H-2′ channels significantly differs from that of the G-2′ channels: for a 6- and 12-s wash, $p < 0.0001$ ($N = 5$).

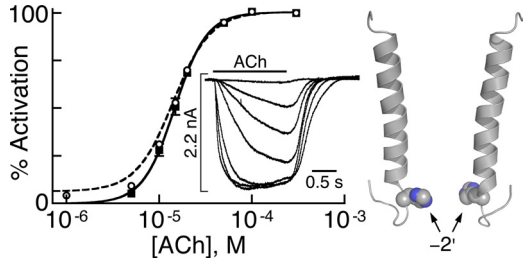

FIGURE 6. **Analysis of macroscopic currents in HEK293T cells expressing chimera H-2′$^{(RRR\rightarrow QDA)}$.** Dose-response curve for chimeras H-2′$^{(RRR\rightarrow QDA)}$ (*continuous black line*) fitted by the Hill equation (Equation 3) to data points obtained from ACh-elicited currents (*black squares*) ($N = 13$ cells). The *inset* shows representative macroscopic currents that increase with the increase in applied ACh concentration (in μM): 5, 10, 15, 20, 50, 100, and 300 (performed at −70 mV at room temperature). The *dashed curve* was fitted to data points that include the ACh-elicited currents plus Zn^{2+}-inhibited leak currents (*open circles*). Fitting of the *dashed curve* was performed by using a two-state allosteric model (Equation 4 under "Experimental Procedures") with $n = 5$ binding sites, microscopic ACh-dissociation constants for the resting (K_Dr) and active (K_Da) states as provided in Table 2, and an equilibrium constant $L = 22.6$ that was determined (with S.E. = 2.3; $N = 12$) using the experimental procedure applied for chimeras H-2′ and H-5′ (explained in the legend to supplemental Fig. S2, *E–H*). On the *right side*, two helical M2 segments of opposite subunits are shown with a space-filling model of histidines at position −2′ (carbon and nitrogen atoms are colored in *gray* and *blue*, respectively).

ents had no effect on the EC_{50} and apparent dissociation constant for ACh when introduced in the chimeric α7–5HT$_{3A}$R, showing that they do not affect macroscopic activation properties (57). Notably, the RRR→QDA mutations were further applied for studying (by single-channel recordings) mechanisms of activation and desensitization in chimeric α7–5HT$_{3A}$ receptors, without or with additional sets of mutations in other regions of the receptor (11, 57, 58). Hence, we decided to introduce the improving mutations in chimera H-2′ and concomitantly replaced Arg-404, Arg-408, and Arg-412 by Gln, Asp, and Ala residues, respectively. We chose chimera H-2′ for this step because its expression level in HEK293T cells (which we used for single-channel recordings) was ~5-fold higher than that of chimera H-5′ (Fig. 2, B_{max} values); and thus, the likelihood of getting a channel-containing patch was higher.

Because the effect of the additional three mutations on the chimeric receptors used here was not known, we analyzed whole-cell current responses in HEK293T cells expressing chimera H-2′$^{(RRR\rightarrow QDA)}$. Fig. 6 (*inset*) demonstrates that the H-2′$^{(RRR\rightarrow QDA)}$ channel population does not desensitize in the presence of saturating ACh concentrations. The ACh-EC_{50} and Hill coefficient determined for chimera H-2′$^{(RRR\rightarrow QDA)}$ were somewhat higher than those for chimera H-2′ (Table 2). However, like chimera H-2′ (and H-5′), chimera H-2′$^{(RRR\rightarrow QDA)}$ displayed significantly lower ACh-EC_{50} and higher Hill coefficients than the "parent" chimeric α7–5HT$_{3A}$R, showing that the three "daughter" chimeras share common macroscopic activation properties (Table 2). A two-state allosteric model

(Fig. 6) indicates that the microscopic ACh dissociation constant derived for the resting state of chimera H-2′$^{(RRR\rightarrow QDA)}$ (K_Dr) is very similar to that of chimera H-2′ (Table 2). Nevertheless, the microscopic ACh dissociation constant derived for the active state (K_Da) of chimera H-2′$^{(RRR\rightarrow QDA)}$ was ~3-fold higher than that of chimera H-2′ and, more importantly, ~8-fold higher than the microscopic ACh dissociation constant derived previously for the desensitized state of the α7–5HT$_{3A}$R (K_Dd) (55) (Table 2). Together, these observations strongly indicate that the conducting channel conformation of chimera H-2′$^{(RRR\rightarrow QDA)}$ corresponds to the active conformation but not to a ("pathologically opened") desensitized state that should have had severalfold higher affinity for ACh. As such, single-channel closing events of chimera H-2′$^{(RRR\rightarrow QDA)}$ could not be attributed to desensitization.

Recordings of single-channel currents from cell-attached patches were performed here at −70 mV using 10 μM Zn^{2+}, a concentration that is 10 times lower than the Zn^{2+} inhibition constant (K_i) previously determined for the open state of chimera H-2′ (100 μM at −70 mV; see Supporting Information of Ref. 21). Using such a low Zn^{2+} concentration (with 1 mM ACh) inside the recording pipette aimed at minimizing the likelihood of blocking the channel for long durations in a nonconducting conformation.

Fig. 7*A* shows single-channel openings from chimera H-2′$^{(RRR\rightarrow QDA)}$ that appear, in the absence of Zn^{2+}, as isolated openings (*upper trace*), bursts of brief and long openings spaced by relatively long closing periods (*middle trace*), and long bursts with shorter closing times (*lower trace*). The distribution of open times within the bursts was fitted with a single exponential, whereas the distribution of closed times was best described by the sum of two exponential components (Fig. 8*A*, decay time constants τ_O, τ_{C1}, and τ_{C2}). In the presence of Zn^{2+}, the channel behaved much differently (Fig. 7*B*); the single-channel currents showed bursts with an increased open channel noise, rapid fluctuations (flickers) in the open channel currents, and a bimodal behavior. One behavioral mode ("Mode-1") displayed prolonged channel openings, which were interrupted by many flickers that could not be fully resolved as rectangular steps at the filtration bandwidth that we used (1 kHz) (*e.g.* Fig. 7*B*, *upper trace*). The second behavioral mode, "Mode-2," displayed openings that were frequently interrupted by transitions to a nonconducting state, which probably indicate fully resolved blocking events that reached the base line (*e.g.* Fig. 7*B, middle* and *lower traces*). Mode-2 could sometimes be observed within the same burst together with Mode-1 (*e.g.* Fig. 7*B, middle trace*) or as separate bursts (*e.g. lower trace*). The distribution of open times in Mode-1 is best described by the sum of two exponential components, whereas the distribution of closed times in this mode is best fitted with a single exponential (Fig. 8*B*). Likewise, the distributions of the open and closed times in Mode-2 were best fitted with two and single exponential components, respectively (Fig. 8*C*). Note that in all the cases where the fit included two exponentials, the contribution of the component that provided longer times did not exceed 10% (legend to Fig. 8). A simple two-state model describes the blocking process in kinetic terms as shown in Scheme 1,

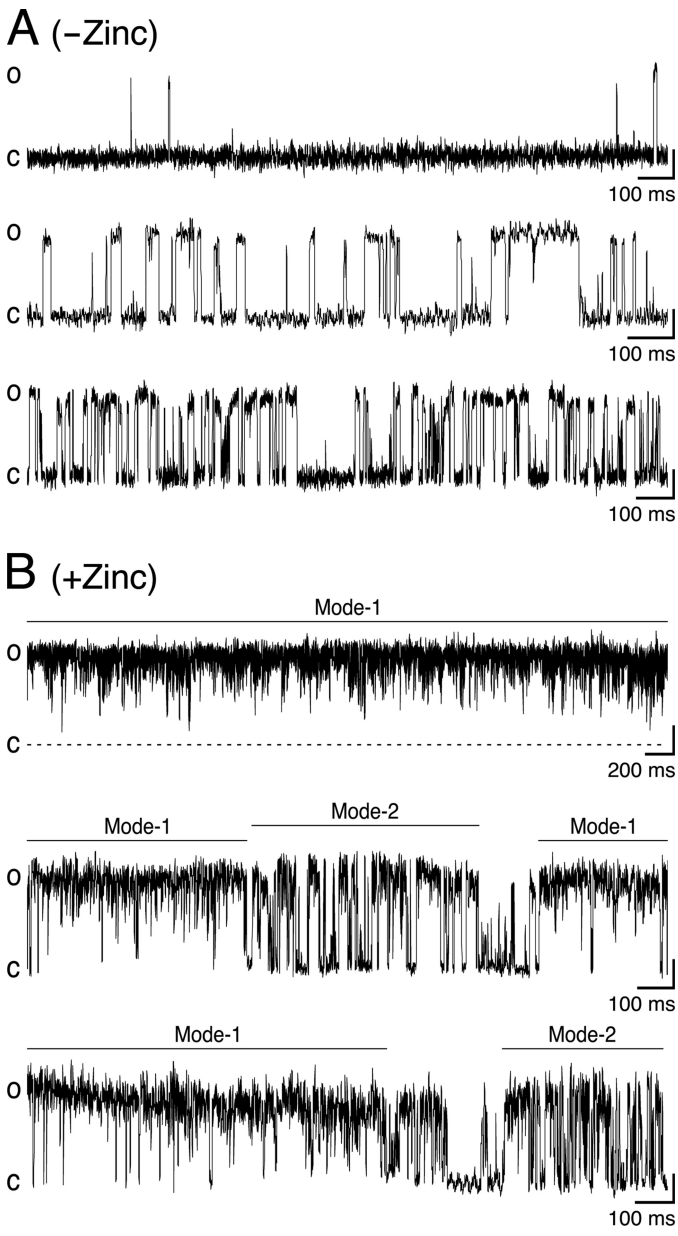

FIGURE 7. **Effect of Zn^{2+} ions on the single-channel activity of chimera H-2′$^{(RRR\rightarrow QDA)}$.** Representative recordings from cell-attached patches in the absence (*A*) or presence (*B*) of 10 μM Zn^{2+} (in the pipette solution). In both cases, the pipette also contained 1 mM ACh. The closed state level is indicated by *c*; the open state level is indicated by *o*. Recordings were performed at −70 mV at room temperature.

$$C \longleftrightarrow O \underset{k_{-Zn}}{\overset{[Zn]k_{+Zn}}{\rightleftharpoons}} OB$$

SCHEME 1

where C is the closed state, O is the open state, OB is the open-blocked state, [Zn] is the concentration of Zn^{2+}, and k_{+Zn} (s^{-1} M^{-1}) and k_{-Zn} (s^{-1}) are the association and dissociation rate constants for Zn^{2+}, respectively. As the rate of open-channel blocking depends on the concentration of Zn^{2+}, [Zn]k_{+Zn} is the actual transition rate for the forward reaction. The equilibrium dissociation constant, K_D, for the blocking reaction (59) is pro-

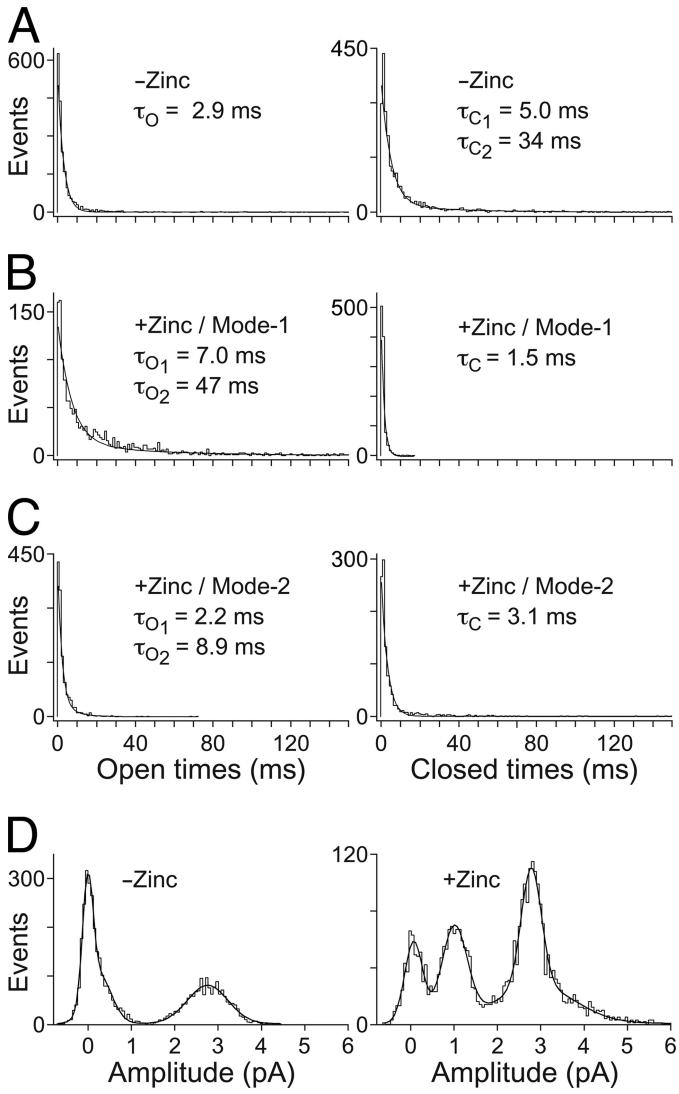

FIGURE 8. **Single-channel properties of chimera H-2′$^{(RRR\rightarrow QDA)}$.** *A–C*, histograms of distributions of open (*left*) and closed (*right*) times measured without or with Zn^{2+} as indicated in the panels. The conditions of single-channel recording are detailed in the legend to Fig. 7. The best fit decay constants are provided within the panels; these τ_O and τ_C values correspond to the mean open and mean closed times, respectively. Note that the long time exponential components τ_{C2} (under −*Zinc*), τ_{O2} (under +*Zinc/Mode-1*) and τ_{O2} (under +*Zinc/Mode-2*) are 5.5, 9, and 6.5% of the contribution (fit span), respectively. *D*, event amplitude histograms for currents recorded in the absence of Zn^{2+} (*left*; $N = 3$ patches) or in the presence of Zn^{2+} (*right*; $N = 4$ patches). The event amplitude histograms were fitted with three Gaussian functions.

vided by the k_{-Zn}/k_{+Zn} ratio. We have used the methodology of Lester and co-workers (60) to determine the values of the rate constants based on a single concentration of an open-channel blocker. As such, $k_{+Zn} = \Delta(1/t)/[Zn]$, and t is the mean open time that is equal to the decay time constants, τ_O or τ_{O1}, in the absence or presence of 10^{-5} M Zn^{2+}, respectively (Fig. 8). Therefore, in the case of Mode-2, $k_{+Zn} = 1.1{\cdot}10^7\ s^{-1}\ M^{-1}$ (calculation detailed under "Experimental Procedures"). The average residence time of Zn^{2+} in the pore throughout Mode-2 is provided by the mean closed time, τ_C, which is equal to $1/k_{-Zn}$. So, $k_{-Zn} = 1/\tau_C = 323\ s^{-1}$, and the K_D of Zn^{2+} binding to the pore during Mode-2 is thus ~29 μM. This value is ~3.5 times lower than that measured previously for the open state of chimera H-2′ (100 μM at −70 mV; see Supporting Information of Ref. 21). We could not employ this calculation in the case of Mode-1, which displays flickery behavior attributed to fast blocking events. This is because, within the recording limitations, many blocking events did not pass the half-amplitude threshold, and thus the long recorded "openings" mask a large number of potential rapid openings and blocking events. Yet, we analyzed the distributions of open and close times of Mode-1 taking into account the resolved and unresolved blocking events that did pass the 50% amplitude. As such, the mean open and closed times of Mode-1 are actually overestimated (τ_{O1}, τ_{O2}, and τ_C, in Fig. 8*B*), but nevertheless, they have a heuristic value as discussed below.

Gaussian fit of amplitude distribution measured in the absence of Zn^{2+} indicates a dominant conducting state with current amplitude of 2.8 pA (Fig. 8*D*, *left*). We did not observe any current fluctuations in a stepwise fashion between different levels (steps) of equal size, which indicates that only one channel was present in each patch. Under the same recording conditions but in the presence of Zn^{2+}, two conducting states dominate as follows: one having a current amplitude of 2.9 pA and another has an amplitude of 1.0 pA (Fig. 8*D*, *right*). As mentioned above, many flickers in Mode-1 are unresolved due to our filtration conditions. Hence, the reduced amplitudes of these unresolved events were not taken into account in the analysis of amplitude distribution, which therefore includes only fully resolved events.

DISCUSSION

It is shown here that the nondesensitizing H-5′ and H-2′ pLGICs interconvert between two dominant conformations, a resting state and an active state (discussed under "Results"). In these pLGICs, the cytoplasmic side of the transmembrane channel domain was equipped with metal-binding sites organized around the ion permeation pathway as a ring that consists of five imidazole groups. As this five-imidazole ring is accessible to water in the pore, Zn^{2+} applied externally onto activated (opened) channels interacts with the ring and thus is capable of blocking the open pore of chimeras H-5′ and H-2′ (Figs. 4 and 5*A* and supplemental Fig. S3*A* and Fig. S2, *A* and *B*). Such a blockage (~90% of the population) is not seen in chimeras that contain glycines instead of histidines (Fig. 5*B* and supplemental Fig. S3*B* and Fig. S2, *C* and *D*). It indicates that Zn^{2+} blocks the opened channels of chimeras H-5′ and H-2′ by interacting specifically with the inserted five-histidine ring.

Washing of ACh from open-blocked channels removes it completely from its binding sites and triggers receptor deactivation, regardless of the presence of zinc (Fig. 5 and supplemental Fig. S3). One may argue, however, that ACh could not readily be removed from open-blocked receptors when perfusing the oocyte with a Zn^{2+}-containing solution; this is because stabilization of the channel in an open conformation by an open-pore blocker might "lock" the agonist in its binding pockets. If so, ACh could potentially remain bound to its binding pockets at the end of the application of the Zn^{2+}-containing solution (Fig. 5*A* and supplemental Fig. S3*A*). However, we exclude this possibility because bound Zn^{2+} does not allosterically increase the binding affinity of chimeras H-5′ and

H-2′ for ACh or nicotine (Fig. 2; Table 1). We thus conclude that the loss of current seen upon ACh reapplication after the first wash in Fig. 5*A* (and supplemental Fig. S3*A*) cannot reflect a channel subpopulation that is still blocked in the active (ACh-liganded) open state. This conclusion is strongly supported by the fact that Zn^{2+} could readily dissociate from open-blocked channels and be removed to allow for full recovery of the response upon ACh reapplication (Fig. 4). It is apparent that upon washing out both ACh and Zn^{2+} simultaneously, Zn^{2+} dissociates from the pore faster than ACh does from its binding sites, thereby allowing the channels to deactivate completely and to enter a reactivatable (resting) state. This conclusion well coincides with the findings that the microscopic ACh dissociation constant characterized for the active state of chimeras H-5′ and H-2′ (K_Da values of 9.4 and 4.4 μM, respectively; Table 2) is lower than the Zn^{2+} inhibition constant determined for the open state of these chimeras (K_i values of 30 and 80 μM, respectively) (21), *i.e.* the active open state has higher affinity for ACh than for Zn^{2+}.

One may also argue that the macroscopic currents actually reflect a population of states through which the channel could transit, so spontaneously opened channels that become blocked by Zn^{2+} might contribute to the unrecovered subpopulation (*i.e.* to the reduced amplitude in Fig. 5*A* and supplemental Fig. S3*A*). We argue against the latter possibility because the inhibitory effect of Zn^{2+} on spontaneously opened channels completely disappears within less than 3 s of wash (*e.g.* Fig. 5*A*, current trace returns from point *c* to the base line). Because in these experiments Zn^{2+} was washed out of the application bath for at least 6 s before reactivation (by ACh), it is clear that the channel population did not contain Zn^{2+}-blocked spontaneously opened channels at the time of ACh reapplication. It is also evident that channels having spontaneous activity do not become stabilized by trapped Zn^{2+}, otherwise the leak currents would not have returned to the base line after 3 s of wash (Fig. 5*A* and supplemental Fig. S3*A* and Fig. S2, *E* and *F*). Furthermore, no progressive accumulation of spontaneously active channels in the open-blocked state or in any other potentially blocked state was observed when exposing H-5′ channels to Zn^{2+} for 3 min (21). Notably, the inability to reopen is specific to the five-histidine ring introduced at the intracellular side of the pore, because no loss of current was observed in similar experiments performed with the control Gly-containing chimeras (G-5′ and G-2′) (Fig. 5, *B* and *C* and supplemental Fig. S3*B*).

Because ACh could dissociate from opened Zn^{2+}-blocked channels (as discussed above), washing of ACh away from active H-5′ or H-2′ channels prior to Zn^{2+} removal most likely triggered the process of receptor deactivation even when Zn^{2+} was still bound within the pore. As such, the currents that are missing upon reactivation with ACh (Fig. 5*A* and supplemental Fig. S3*A*) reasonably correspond to channels that could not reopen because of strong Zn^{2+} binding in a state reached during the process of deactivation. We infer that in these unrecovered channels, a Zn^{2+} ion interacts with the five-histidine ring on the way of the channel to close. Shutting the cytoplasmic side of the transmembrane pore on the Zn^{2+} ion would reasonably lead to Zn^{2+} ion trapping and stabilization of a nonconducting state. Such a process is feasible because of the following: (i) upon deactivation, the intracellular side of the pore-lining segments most likely moves toward the axis of ion permeation pathway to constrict the ring of five imidazoles, and (ii) the orientation of the histidines is preserved during the deactivation process. The constriction of the pore is illustrated in Fig. 9, *A* and *B*, and the effect of pore constriction on Zn^{2+} ion coordination within the pore is illustrated in Fig. 9, *C* and *D*. Zn^{2+} binding in the open active state probably involves electrostatic interactions with two adjacent histidines (Fig. 9*C*). Upon deactivation, the distances between the histidines and the axis of ion permeation pathway as well as between adjacent histidines get smaller; *i.e.* the histidines come together. The subsequent decrease in the diameter of the five-imidazole ring enables stronger Zn^{2+} ion coordination (Fig. 9*D*). Such a metal ion coordination is yet largely different from that seen in metallo-enzymes (61, 62) because of the channel pentagonal geom-

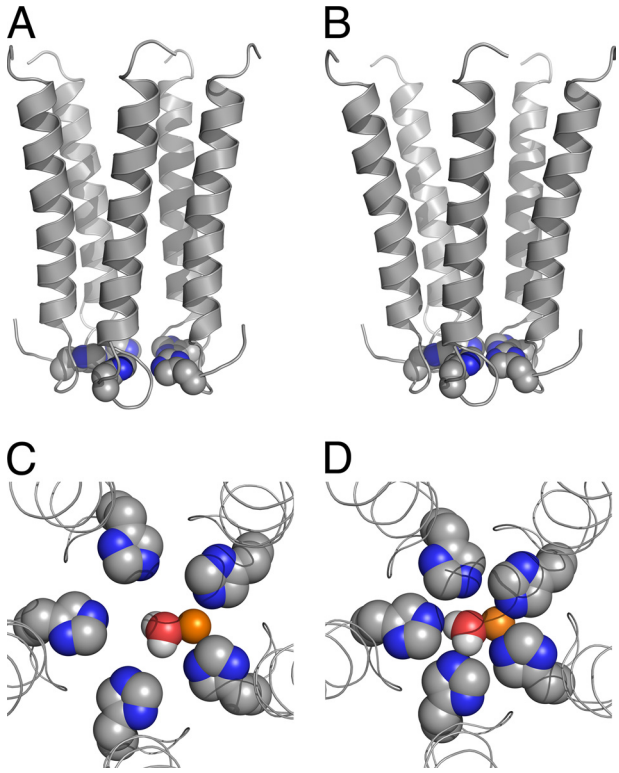

FIGURE 9. **Putative Zn^{2+} ion coordination within the ion channel pore.** *A* and *B*, side views of the five pore-lining helices (M2s) of the putative active (*A*) and deactivated (*B*) channel conformations of chimera H-5′. *C* and *D*, *top views* of the putative activation/deactivation gate of chimera H-5′, which consists of five histidines organized around the axis of ion permeation pathway as a ring that accommodates a Zn^{2+} ion with an equatorially bound water molecule; shown are the putative active (*C*) and deactivated (*D*) gate conformations. Space-filling model of the histidines, Zn^{2+}, and water are shown with the following colors: carbon, *gray*; nitrogen, *blue*; oxygen, *red*; hydrogen, *white*; Zn^{2+}, *orange*. In the open pore model (*C*), the center-to-center distance between docked Zn^{2+} and the Nϵ atoms of the imidazole groups is 3.2 Å, whereas in the closed pore model (*D*) it is 2.3–2.4 Å. In both models the water oxygen is 2.3 Å away from the Zn^{2+} ion (center-to-center). Note that in water a Zn^{2+} ion is surrounded by a first hydration shell of six water molecules (87), so additional water molecules are probably bound to the Zn^{2+} ion above and below the shown plane. Notably, the models depicted here probably represent one of several possible different conformations that histidines may adopt, whereas Zn^{2+} itself can presumably induce changes in the histidine conformation.

etry, which allows a Zn^{2+} ion to directly interact only with two histidines concomitantly.

The flickery behavior of the single channel seen under Mode-1 (Fig. 7*B*) is reminiscent of the flickers observed when the activity of a single muscle nAChR was measured, at <1-kHz filtration bandwidth, in the presence of the local anesthetic compounds QX-222 (63) or benzocaine (64). These compounds are well characterized open-channel blockers of nAChRs (60, 65, 66). Likewise, the flickers induced here by a low Zn^{2+} concentration (Mode-1) imply fast blocking events that coincide with the short mean closed time for Mode-1 (1.5 ms). Interestingly, the mean open times of Mode-1 (7.0 and 47 ms) are considerably longer than that observed in recordings without Zn^{2+} (2.9 ms). As stated under "Results," these mean closed and open times of Mode-1 are probably overestimated. Yet, they indicate that at a low Zn^{2+} concentration, chimera H-2′$^{(RRR\rightarrow QDA)}$ fluctuates between the open (O) and open-blocked (OB) states (O ↔ OB), and Zn^{2+} interferes with channel closing. Because the channel continues to conduct between fast blocking events, we argue that the low Zn^{2+} concentration (one-tenth of Zn^{2+}-K_i of chimera H-2′) prolongs the lifetime of the open state. Such prolongation of open times by an open-channel blocker (tetraethylammonium) was also observed in ATP-sensitive potassium channels (67). In line with this conclusion, the single-channel open probability in Mode-1 is very high ($P_o \approx 0.96$) compared with Mode-2 and recordings without Zn^{2+} ($P_o \approx 0.42$ and $P_o \approx 0.3$, respectively). Note that the high P_o of Mode-1 is somewhat overestimated due to many fast blocking events that were filtered out by our recording conditions. Taken together, Mode-1 behavior corroborates previous inferences that were made on the basis of macroscopic current measurements (21), *i.e.* a large population of H-2′ channels could be shifted from a nonconducting OB state to long lasting O ↔ OB fluctuations accompanied with high conductance. This process was reflected by large macroscopic tail currents seen when the external Zn^{2+} concentration was rapidly reduced under very negative membrane potentials that increased the driving force for Zn^{2+} ion movement toward the five-histidine ring (21).

The mean closed time of Mode-2 (3.1 ms) is shorter than that measured without Zn^{2+} (5 ms), indicating that the channel openings in Mode-2 are interrupted by fully resolved slow blocking events that render the channel nonconducting. The time constants τ_C of Mode-1 and Mode-2 correspond to the average residence time for Zn^{2+} in the pore, and it is longer during Mode-2. Hence, in analogy to the macroscopic currents, we suggest that Mode-2 reflects the process of Zn^{2+} ion trapping upon deactivation. Yet, it appears that the co-presence of a very low Zn^{2+} concentration together with high ACh concentration in the single-channel recording pipette prevented the channel from entering into a sustained nonconducting blocked state.

The induction of a subconducting state by Zn^{2+} (Fig. 8*D*, *right*) implies that Zn^{2+} not only blocks the "fully" opened channel but also allows the channel to assume an open-blocked state having a smaller pore diameter. Relief of the latter state from the block probably causes the appearance of a subconductance. Taken together with the analysis of time distributions, we infer that Zn^{2+} acts as a "foot in the door" that does not let the single channel enter a completely deactivated-closed conformation and delays the eventual closing of the gate. This Zn^{2+}-stabilized partially open/partially closed conformation might be analogous to the pre-open state recently shown to occur in the muscle nAChR (68, 69).

Notably, the results presented here are in full agreement with earlier studies of Karlin and co-workers (19, 20, 33) who showed that the activation gate of the muscle nAChR is located at the cytoplasmic side of the channel pore. Our current results also corroborate the previous conclusions of Paas *et al.* (21) regarding the location of the activation gate in the chimeric ACh-serotonin receptor, although one may still argue that the histidines created a second gate additionally to the native gate whose activity is masked by Zn^{2+} blockage. We exclude this possibility because the inserted histidines were accessed by external Zn^{2+} ions even before activation (21), indicating that in the resting state of our chimeras there is no interference for Zn^{2+} ion movement all the way to the bottom of the pore. It is also not likely that there is a gate below the five-histidine ring because the sequence upstream to position −5′ is located farther away from the ion permeation pathway, as it needs to connect to M1 (Fig. 1*B*). On the other hand, the substituting histidines most likely created a gate instead of the native gate, nearly at the same place. Reasonable candidates for creating a native gate at the bottom of the pore of the donor receptor ($5HT_{3A}R$) are five glutamates at positions −1′, whose side chains are organized as a ring around the axis of ion permeation pathway (70). Note that in our chimeras, glycine residues replace these glutamates (Fig. 1*C*). Because the van der Waals volumes of Glu and His are quite close (109 *versus* 118 $Å^3$, respectively) (71), it seems that there is sufficient space at the bottom of the pore of the chimeras to accommodate a ring of five histidines without altering the orientation of the M2 helices significantly, if at all.

Recently, the x-ray crystal structures of two different pLGICs from distantly related prokaryotes were determined at atomic resolution. The first, ELIC (from *Erwinia chrysanthemi*, a Gram-negative bacillus belonging to the family Enterobacteriaceae), displays a closed pore conformation in the crystal (30). The second, GLIC (from the cyanobacterium *Gloeobacter violaceus*), displays a potentially open pore conformation in the crystal (31, 32). It appears that the funnel-like structure of GLIC is reminiscent of the open pore shape previously suggested for eukaryotic pLGICs based on functional studies (19, 21–23, 33, 72). Superimposition of the crystal structures of ELIC and GLIC suggests that rigid-body tilting of the pore-lining helices gate the channel (31, 32), in accordance with previous inference based on functional studies done with a eukaryotic pLGIC (21). However, the crystal structure of ELIC shows that the upper (extracellular) side of the channel pore is too narrow to allow ions to pass, and the bottom (intracellular) side of the pore is much wider (30). Based on the assumption that ELIC and GLIC share a similar gating mechanism, it was inferred that closing of these prokaryotic pLGICs is accompanied by widening of the intracellular side of the pore (see supplemental movies in Hilf and Dutzler (31)). Conversely, agonist dissociation, which triggers the deactivation process in the eukaryotic pLGICs explored here, is accompanied with narrowing of the intracel-

lular side of the pore. It should be emphasized that the affinity of the constricted state of the chimeras studied here for Zn^{2+} is not less than the affinity of their open state for Zn^{2+}. This finding supports our plausible inference that the diameter of the five-histidine ring does not increase upon closing of chimeras H-5′ and H-2′, unlike an ELIC-like closing that should have increased the diameter of the five-histidine ring and weakened the interactions with Zn^{2+}. One may argue, however, that if Zn^{2+} ions flow into the cell, a high concentration of Zn^{2+} would remain in the vicinity of the five-histidine ring upon an ELIC-like pore closing. In such a case, upon re-activation, a GLIC-like opening might result in trapping of Zn^{2+} and inability of the channel to conduct. We exclude these possibilities in the case of our eukaryotic chimeras because an increase in the intracellular Zn^{2+} concentrations during the single-channel recordings should have gradually increased the portion of Mode-2 over Mode-1 and prolonged the nonconducting periods. The single-channel recordings show that such processes did not occur. Moreover, if Zn^{2+} ions were flowing into the cell, the channel population in Fig. 4 would not have recovered entirely because of Zn^{2+} acting from the cytoplasm. This did not happen (Fig. 4) even at very negative membrane potentials that increase the driving force for Zn^{2+} inflow (21).

Two possible explanations may account for the difference between the eukaryotic and prokaryotic pLGICs. According to the first possibility, the crystallization conditions may have forced ELIC into a desensitized-like low energy conformation, so the constricted ring of five phenylalanines that line the extracellular end of the ELIC pore may actually corresponds to a desensitization gate rather than an activation/deactivation gate. This possibility coincides with Wilson and Karlin (20) who localized a desensitization gate topologically above the activation gate in the muscle nAChR, and with Purohit and Grosman (73) who suggested that the activation and desensitization gates are distinct entities. According to the second possibility, both the location of the activation/deactivation gate and the direction of the tilting motions that open and close this gate in eukaryotic pLGICs may be different from those of ELIC and GLIC. Various functional and affinity-labeling studies support this possibility. When applied externally at low concentrations in functional (electrophysiological) experiments, the local anesthetic tetracaine acts as a noncompetitive antagonist by blocking the pore of both the open and resting states of muscle-type (74) and neuronal (75) nAChRs. In the absence of an agonist, tetracaine binds to the muscle-type *Torpedo* nAChR with 100-fold higher affinity than in the presence of an agonist, *i.e.* tetracaine preferentially binds to the resting state of the *Torpedo* receptor (76). The high-affinity binding site for tetracaine in the resting *Torpedo* nAChR was identified by photoaffinity labeling experiments, which were performed in the absence of an agonist using either [^{3}H]tetracaine (77) or unlabeled tetracaine to inhibit the photoincorporation of other pore blockers, analogs of 3-trifluoromethyl-3-(*m*-^{125}I-iodophenyl)diazirine (78). It was found that residues located at positions 13′, 9′, and 5′ in various pore-lining segments of the *Torpedo* nAChR contribute to a specific site for tetracaine. These positions in the *Torpedo* nAChR are respectively located two, three, and four helical turns below position 20′ (Protein Data Bank code 1OED) (18). Position 20′ appears to be at the same topological level of the ring of five phenylalanines that was implied to constrict and close the ELIC pore (see sequence alignment in supplemental Fig. S1*a* of Ref. 30 and Protein Data Bank code 2VL0). It thus appears that to block the pore of resting nAChRs, externally applied tetracaine should pass through position 20′ of the pore. This excludes the presence of an ELIC-like steric hindrance in the resting conformation of the aforementioned eukaryotic nAChRs.

Notably, differences in gating motions of pore-lining helices exist in potassium channels, despite the high tertiary and quaternary structural conservation of their pore domain. Crystal structures of two bacterial potassium channels, KcsA (in a closed conformation) (79) and MthK (in an open conformation) (80), imply that channel opening involves a hinge bending motion at a conserved glycine in the middle of the inner pore helices (81). In contrast, in eukaryotic Shaker family Kv channels, both functional studies and x-ray crystallography suggest that opening involves bending of the inner pore helices at a proline motif (Pro-Xaa-Pro) that is not found in bacterial K^+ channels and is located closer to the intracellular side of the inner pore helices (82–84). These differences lead to variations in the open pore diameter, which is narrower in the Shaker Kv1.2 channel.

As to the gating mechanism of prokaryotic pLGICs, this still has to be functionally probed to ascertain the relevance of the structural states seen in detergent (and crystallization substances) to function of the receptors in the membrane.

In conclusion, here we have provided functional evidence that agonist dissociation, which triggers the receptor transition from the active open conformation to the resting closed conformation, causes the intracellular end of the pore-lining segments of an ACh-serotonin receptor chimera (a eukaryotic pLGIC) to move toward the 5-fold axis of symmetry so as to constrict the pore at its cytoplasmic side. We infer that such a constriction motion ultimately results in deactivation and obstruction of the ion permeation pathway.

Acknowledgments—We thank Drs. Arthur Karlin and Bernard Attali for critical reading of the manuscript and discussions and Dr. Alon Korngreen for technical help.

REFERENCES

1. Karlin, A. (2002) *Nat. Rev. Neurosci.* **3,** 102–114
2. Lester, H. A., Dibas, M. I., Dahan, D. S., Leite, J. F., and Dougherty, D. A. (2004) *Trends Neurosci.* **27,** 329–336
3. Betz, H., and Laube, B. (2006) *J. Neurochem.* **97,** 1600–1610
4. Sine, S. M., and Engel, A. G. (2006) *Nature* **440,** 448–455
5. Taylor, P., Talley, T. T., Radic', Z., Hansen, S. B., Hibbs, R. E., and Shi, J. (2007) *Biochem. Pharmacol.* **74,** 1164–1171
6. Olsen, R. W., and Sieghart, W. (2009) *Neuropharmacology* **56,** 141–148
7. Changeux, J. P. (2009) *C. R. Biol.* **332,** 421–425
8. Kash, T. L., Jenkins, A., Kelley, J. C., Trudell, J. R., and Harrison, N. L. (2003) *Nature* **421,** 272–275
9. Bouzat, C., Gumilar, F., Spitzmaul, G., Wang, H. L., Rayes, D., Hansen, S. B., Taylor, P., and Sine, S. M. (2004) *Nature* **430,** 896–900
10. Mercado, J., and Czajkowski, C. (2008) *J. Biol. Chem.* **283,** 15250–15257
11. Bouzat, C., Bartos, M., Corradi, J., and Sine, S. M. (2008) *J. Neurosci.* **28,** 7808–7819
12. Wiltfong, R. E., and Jansen, M. (2009) *J. Neurosci.* **29,** 1626–1635

13. Lee, W. Y., Free, C. R., and Sine, S. M. (2009) *J. Neurosci.* **29,** 3189–3199
14. Pless, S. A., and Lynch, J. W. (2009) *J. Biol. Chem.* **284,** 15847–15856
15. Perkins, D. I., Trudell, J. R., Crawford, D. K., Asatryan, L., Alkana, R. L., and Davies, D. L. (2009) *J. Biol. Chem.* **284,** 27304–27314
16. Pless, S. A., and Lynch, J. W. (2009) *J. Biol. Chem.* **284,** 27370–27376
17. Unwin, N. (1995) *Nature* **373,** 37–43
18. Miyazawa, A., Fujiyoshi, Y., and Unwin, N. (2003) *Nature* **423,** 949–955
19. Wilson, G. G., and Karlin, A. (1998) *Neuron* **20,** 1269–1281
20. Wilson, G., and Karlin, A. (2001) *Proc. Natl. Acad. Sci. U.S.A.* **98,** 1241–1248
21. Paas, Y., Gibor, G., Grailhe, R., Savatier-Duclert, N., Dufresne, V., Sunesen, M., de Carvalho, L. P., Changeux, J. P., and Attali, B. (2005) *Proc. Natl. Acad. Sci. U.S.A.* **102,** 15877–15882
22. Cymes, G. D., Ni, Y., and Grosman, C. (2005) *Nature* **438,** 975–980
23. Cymes, G. D., and Grosman, C. (2008) *Nat. Struct. Mol. Biol.* **15,** 389–396
24. Taly, A., Delarue, M., Grutter, T., Nilges, M., Le Novère, N., Corringer, P. J., and Changeux, J. P. (2005) *Biophys. J.* **88,** 3954–3965
25. Taly, A., Corringer, P. J., Grutter, T., Prado de Carvalho, L., Karplus, M., and Changeux, J. P. (2006) *Proc. Natl. Acad. Sci. U.S.A.* **103,** 16965–16970
26. Cheng, X., Wang, H., Grant, B., Sine, S. M., and McCammon, J. A. (2006) *PLoS Comput. Biol.* **2,** e134
27. Ivanov, I., Cheng, X., Sine, S. M., and McCammon, J. A. (2007) *J. Am. Chem. Soc.* **129,** 8217–8224
28. Cheng, M. H., Cascio, M., and Coalson, R. D. (2007) *Proteins* **68,** 581–593
29. Liu, X., Xu, Y., Li, H., Wang, X., Jiang, H., and Barrantes, F. J. (2008) *PLoS Comput. Biol.* **4,** e19
30. Hilf, R. J., and Dutzler, R. (2008) *Nature* **452,** 375–379
31. Hilf, R. J., and Dutzler, R. (2009) *Nature* **457,** 115–118
32. Bocquet, N., Nury, H., Baaden, M., Le Poupon, C., Changeux, J. P., Delarue, M., and Corringer, P. J. (2009) *Nature* **457,** 111–114
33. Pascual, J. M., and Karlin, A. (1998) *J. Gen. Physiol.* **111,** 717–739
34. Sunesen, M., de Carvalho, L. P., Dufresne, V., Grailhe, R., Savatier-Duclert, N., Gibor, G., Peretz, A., Attali, B., Changeux, J. P., and Paas, Y. (2006) *J. Biol. Chem.* **281,** 14875–14881
35. Celie, P. H., van Rossum-Fikkert, S. E., van Dijk, W. J., Brejc, K., Smit, A. B., and Sixma, T. K. (2004) *Neuron* **41,** 907–914
36. Karlin, A. (1967) *J. Theor. Biol.* **16,** 306–320
37. Eiselé, J. L., Bertrand, S., Galzi, J. L., Devillers-Thiéry, A., Changeux, J. P., and Bertrand, D. (1993) *Nature* **366,** 479–483
38. Dang, H., England, P. M., Farivar, S. S., Dougherty, D. A., and Lester, H. A. (2000) *Mol. Pharmacol.* **57,** 1114–1122
39. Miller, P. S., Topf, M., and Smart, T. G. (2008) *Nat. Struct. Mol. Biol.* **15,** 1084–1093
40. Brejc, K., van Dijk, W. J., Klaassen, R. V., Schuurmans, M., van Der Oost, J., Smit, A. B., and Sixma, T. K. (2001) *Nature* **411,** 269–276
41. Chang, C. C., and Lee, C. Y. (1966) *Br. J. Pharmacol. Chemother.* **28,** 172–181
42. Lester, H. A. (1970) *Nature* **227,** 727–728
43. Changeux, J. P., Kasai, M., and Lee, C. Y. (1970) *Proc. Natl. Acad. Sci. U.S.A.* **67,** 1241–1247
44. Harel, M., Kasher, R., Nicolas, A., Guss, J. M., Balass, M., Fridkin, M., Smit, A. B., Brejc, K., Sixma, T. K., Katchalski-Katzir, E., Sussman, J. L., and Fuchs, S. (2001) *Neuron* **32,** 265–275
45. Samson, A., Scherf, T., Eisenstein, M., Chill, J., and Anglister, J. (2002) *Neuron* **35,** 319–332
46. Hansen, S. B., Sulzenbacher, G., Huxford, T., Marchot, P., Taylor, P., and Bourne, Y. (2005) *EMBO J.* **24,** 3635–3646
47. Bourne, Y., Talley, T. T., Hansen, S. B., Taylor, P., and Marchot, P. (2005) *EMBO J.* **24,** 1512–1522
48. Celie, P. H., Kasheverov, I. E., Mordvintsev, D. Y., Hogg, R. C., van Nierop, P., van Elk, R., van Rossum-Fikkert, S. E., Zhmak, M. N., Bertrand, D., Tsetlin, V., Sixma, T. K., and Smit, A. B. (2005) *Nat. Struct. Mol. Biol.* **12,** 582–588
49. Dutertre, S., Ulens, C., Büttner, R., Fish, A., van Elk, R., Kendel, Y., Hopping, G., Alewood, P. F., Schroeder, C., Nicke, A., Smit, A. B., Sixma, T. K., and Lewis, R. J. (2007) *EMBO J.* **26,** 3858–3867
50. Anand, R., Peng, X., and Lindstrom, J. (1993) *FEBS Lett.* **327,** 241–246
51. Corringer, P. J., Galzi, J. L., Eiselé, J. L., Bertrand, S., Changeux, J. P., and Bertrand, D. (1995) *J. Biol. Chem.* **270,** 11749–11752
52. Revah, F., Bertrand, D., Galzi, J. L., Devillers-Thiéry, A., Mulle, C., Hussy, N., Bertrand, S., Ballivet, M., and Changeux, J. P. (1991) *Nature* **353,** 846–849
53. Labarca, C., Nowak, M. W., Zhang, H., Tang, L., Deshpande, P., and Lester, H. A. (1995) *Nature* **376,** 514–516
54. Monod, J., Wyman, J., and Changeux, J. P. (1965) *J. Mol. Biol.* **12,** 88–118
55. Grutter, T., Prado de Carvalho, L., Le Novère, N., Corringer, P. J., Edelstein, S., and Changeux, J. P. (2003) *EMBO J.* **22,** 1990–2003
56. Kelley, S. P., Dunlop, J. I., Kirkness, E. F., Lambert, J. J., and Peters, J. A. (2003) *Nature* **424,** 321–324
57. Rayes, D., Spitzmaul, G., Sine, S. M., and Bouzat, C. (2005) *Mol. Pharmacol.* **68,** 1475–1483
58. Rayes, D., De Rosa, M. J., Sine, S. M., and Bouzat, C. (2009) *J. Neurosci.* **29,** 6022–6032
59. Aidley, D. J., and Stanfield, P. R. (1996) *Ion Channels: Molecules in Action*, pp. 225–229, Cambridge University Press
60. Charnet, P., Labarca, C., Leonard, R. J., Vogelaar, N. J., Czyzyk, L., Gouin, A., Davidson, N., and Lester, H. A. (1990) *Neuron* **4,** 87–95
61. Alberts, I. L., Nadassy, K., and Wodak, S. J. (1998) *Protein Sci.* **7,** 1700–1716
62. Higaki, J. N., Fletterick, R. J., and Craik, C. S. (1992) *Trends Biochem. Sci.* **17,** 100–104
63. Neher, E., and Steinbach, J. H. (1978) *J. Physiol.* **277,** 153–176
64. Ogden, D. C., Siegelbaum, S. A., and Colquhoun, D. (1981) *Nature* **289,** 596–598
65. Leonard, R. J., Labarca, C. G., Charnet, P., Davidson, N., and Lester, H. A. (1988) *Science* **242,** 1578–1581
66. Pascual, J. M., and Karlin, A. (1998) *J. Gen. Physiol.* **112,** 611–621
67. Davies, N. W., Spruce, A. E., Standen, N. B., and Stanfield, P. R. (1989) *J. Physiol.* **413,** 31–48
68. Mukhtasimova, N., Lee, W. Y., Wang, H. L., and Sine, S. M. (2009) *Nature* **459,** 451–454
69. Lape, R., Krashia, P., Colquhoun, D., and Sivilotti, L. G. (2009) *J. Physiol.* **587,** 5045–5072
70. Gunthorpe, M. J., and Lummis, S. C. (2001) *J. Biol. Chem.* **276,** 10977–10983
71. Creighton, T. E. (1993) *Proteins: Structure and Molecular Properties,* 2nd Ed., p. 141, W. H. Freeman & Co., New York
72. Akabas, M. H., Kaufmann, C., Archdeacon, P., and Karlin, A. (1994) *Neuron* **13,** 919–927
73. Purohit, Y., and Grosman, C. (2006) *J. Gen. Physiol.* **127,** 703–717
74. Papke, R. L., and Oswald, R. E. (1989) *J. Gen. Physiol.* **93,** 785–811
75. Papke, R. L., Horenstein, B. A., and Placzek, A. N. (2001) *Mol. Pharmacol.* **60,** 1365–1374
76. Blanchard, S. G., Elliott, J., and Raftery, M. A. (1979) *Biochemistry* **18,** 5880–5885
77. Gallagher, M. J., and Cohen, J. B. (1999) *Mol. Pharmacol.* **56,** 300–307
78. Blanton, M. P., McCardy, E. A., and Gallagher, M. J. (2000) *J. Biol. Chem.* **275,** 3469–3478
79. Doyle, D. A., Morais Cabral, J., Pfuetzner, R. A., Kuo, A., Gulbis, J. M., Cohen, S. L., Chait, B. T., and MacKinnon, R. (1998) *Science* **280,** 69–77
80. Jiang, Y., Lee, A., Chen, J., Cadene, M., Chait, B. T., and MacKinnon, R. (2002) *Nature* **417,** 515–522
81. Jiang, Y., Lee, A., Chen, J., Cadene, M., Chait, B. T., and MacKinnon, R. (2002) *Nature* **417,** 523–526
82. del Camino, D., and Yellen, G. (2001) *Neuron* **32,** 649–656
83. Webster, S. M., Del Camino, D., Dekker, J. P., and Yellen, G. (2004) *Nature* **428,** 864–868
84. Long, S. B., Campbell, E. B., and Mackinnon, R. (2005) *Science* **309,** 897–903
85. Sola, M., Bavro, V. N., Timmins, J., Franz, T., Ricard-Blum, S., Schoehn, G., Ruigrok, R. W., Paarmann, I., Saiyed, T., O'Sullivan, G. A., Schmitt, B., Betz, H., and Weissenhorn, W. (2004) *EMBO J.* **23,** 2510–2519
86. Leil, T. A., Chen, Z. W., Chang, C. S., and Olsen, R. W. (2004) *J. Neurosci.* **24,** 11429–11438
87. Díaz, N., Suárez, D., and Merz, K. M., Jr. (2000) *Chem. Phys. Lett.* **326,** 288–292